Acta Biomaterialia 10 (2014) 544–556

Contents lists available at ScienceDirect

Acta Biomaterialia

journal homepage: www.elsevier.com/locate/actabiomat

Enhanced antimicrobial properties, cytocompatibility, and corrosion resistance of plasma-modified biodegradable magnesium alloys

Ying Zhao [a,b], Mohammed Ibrahim Jamesh [b], Wing Kan Li [a], Guosong Wu [b], Chenxi Wang [b], Yufeng Zheng [c], Kelvin W.K. Yeung [a,d,*], Paul K. Chu [b,*]

[a] Department of Orthopaedics & Traumatology, The University of Hong Kong, Pokfulam Road, Hong Kong, China
[b] Department of Physics and Materials Science, City University of Hong Kong, Tat Chee Avenue, Kowloon, Hong Kong, China
[c] State Key Laboratory for Turbulence and Complex System and Department of Materials Science and Engineering, College of Engineering, Peking University, Beijing 100871, China
[d] Shenzhen Key Laboratory for Innovative Technology in Orthopaedic Trauma, The University of Hong Kong Shenzhen Hospital, 1 Haiyuan 1st Road, Futian Distract, Shenzhen, China

ARTICLE INFO

Article history:
Available online 18 October 2013

Keywords:
Magnesium alloy
Biodegradable
Cytocompatibility
Corrosion
Interfaces

ABSTRACT

Magnesium alloys are potential biodegradable materials and have received increasing attention due to their outstanding biological performance and mechanical properties. However, rapid degradation in the physiological environment and potential toxicity limit clinical applications. Recently, special magnesium–calcium (Mg–Ca) and magnesium–strontium (Mg–Sr) alloys with biocompatible chemical compositions have been reported, but the rapid degradation still does not meet clinical requirements. In order to improve the corrosion resistance, a rough, hydrophobic and ZrO_2-containing surface film is fabricated on Mg–Ca and Mg–Sr alloys by dual zirconium and oxygen ion implantation. Weight loss measurements and electrochemical corrosion tests show that the corrosion rate of the Mg–Ca and Mg–Sr alloys is reduced appreciably after surface treatment. A systematic investigation of the in vitro cellular response and antibacterial capability of the modified binary magnesium alloys is performed. The amounts of adherent bacteria on the Zr–O-implanted and Zr-implanted samples diminish remarkably compared to the unimplanted control. In addition, significantly enhanced cell adhesion and proliferation are observed from the Zr–O-implanted sample. The results suggest that dual zirconium and oxygen ion implantation, which effectively enhances the corrosion resistance, in vitro biocompatibility and antimicrobial properties of Mg–Ca and Mg–Sr alloys, provides a simple and practical means to expedite clinical acceptance of biodegradable magnesium alloys.

1. Introduction

Stainless steels, titanium and titanium alloys are the most widely used artificial surgical biomaterials. However, on account of their non-degradability and the mismatch of their mechanical properties with those of human bones, long-term adverse effects or stress shielding may occur after surgery. This may lead to bone loss and a higher risk of implant failure. To avoid this problem, implants made of biodegradable materials are used as alternatives. Among the various biodegradable materials, magnesium alloys have unique biodegradability in the physiological environment, have stimulatory effects on new bone formation and have an elastic modulus similar to that of human bone [1–4]. The major obstacle hampering their clinical use is their rapid degradation inside the human body. Human body fluids and blood plasma contain chloride ions that accelerate corrosion of magnesium alloys, producing hydrogen gas and localized basification [5]. Even though the corrosion resistance of some magnesium alloys can be enhanced by adding aluminum, rare earth elements and heavy metals, the alloyed materials may be not be suitable for biomedical applications due to potential toxicity and pathopoiesis of elements. Since the mechanical properties and corrosion resistance of pure magnesium are unsatisfactory, novel Mg–Ca and Mg–Sr alloys have recently be proposed as alternatives [6,7], but the anti-corrosion properties are still not ideal.

Proper control of the degradation process on magnesium alloys is therefore imperative. Protective coatings have been deposited to inhibit corrosion, and other surface modification techniques have been evaluated as well [8,9]. Ion implantation is an excellent surface modification technique and has been used on various materials to improve their surface properties [10,11]. Compared to conventional coating techniques, ion implantation can introduce a suitable number of ions into the near surface of the materials

* Corresponding authors. Address: Department of Orthopaedics & Traumatology, The University of Hong Kong, Pokfulam Road, Hong Kong, China. Tel.: +852 22554654; fax: +852 28174392 (K.W.K. Yeung). Tel.: +852 34427724; fax: +852 34420542 (P.K. Chu).
E-mail addresses: wkkyeung@hku.hk (K.W.K. Yeung), paul.chu@cityu.edu.hk (P.K. Chu).

1742-7061/$ - see front matter © 2013 Acta Materialia Inc. Published by Elsevier Ltd. All rights reserved.
http://dx.doi.org/10.1016/j.actbio.2013.10.012

to alter the surface properties without creating an abrupt interface so that film delamination is typically not serious. Metals such as titanium and aluminum have been implanted to control the degradation rate of magnesium and its alloys [12–14]. In metal ion implantation, improvement in the corrosion resistance is often related to the formation of a corrosion-resistant metal oxide and dramatically reduced magnesium content in the near surface [15]. In many cases, after metal ion implantation, it is still necessary to modify the sample surface further to enable optimal formation of the metal oxide, and oxygen co-implantation by means of plasma immersion ion implantation (PIII) can yield the optimal effects.

While issues related to rapid surface degradation must be solved, good antibacterial properties and acceptable cytotoxicity are also necessary. In principle, if cytocompatible and antibacterial elements are introduced, the resulting materials also have enhanced cytocompatibility and antibacterial characteristics. Common elements are silver [16], zinc [17] and copper [18], all of which have good antibacterial activity, though an excess amount may cause deleterious effects. Zirconium has good cytocompatibility and antibacterial properties [19–21], and zirconium oxide has been reported to exhibit low toxicity while having the ability to inhibit bacterial colonization on the surface [22–25]. In this work, zirconium and oxygen ion implantation is conducted sequentially to modify Mg–Ca and Mg–Sr alloys and their corrosion resistance, cytocompatibility and antimicrobial characteristics are determined systematically.

2. Experimental details

2.1. Sample preparation

A Mg–Ca (1 wt.% Ca content) alloy ingot was cast from commercial pure magnesium (99.98%) and Ca (99.95%) in a crucible under a mixed atmosphere of SF_6 and CO_2, then extruded into a rod at 210 °C at a reduction ratio of 17 [8]. Mg–Sr (0.5 wt.% Sr content) alloys were prepared from pure magnesium (99.98%) and a Mg–10 wt.% Sr master alloy in a crucible under mixed SF_6 and CO_2. After holding at 740–760 °C for 30 min, the melt was poured into a steel mold preheated to 300 °C [6]. The Mg–Ca and Mg–Sr alloy samples, $10 \times 10 \times 2$ mm^3 in size, were machined from the extruded Mg–Ca rod and as-cast Mg–Sr ingot, mechanically polished up to 1200 grit and ultrasonically cleaned in acetone and ethanol. The resulting magnesium alloy samples were subjected to zirconium ion implantation on an HEMII-80 ion implanter (Plasma Technology Ltd., Hong Kong, China) equipped with a zirconium cathodic arc source. The samples were implanted for 0.5 h at a terminal voltage of 25 kV and a base pressure of 1.5×10^{-3} Pa. Afterwards, oxygen PIII was conducted on the GPI-100 ion implanter (Plasma Technology Ltd., Hong Kong, China). Oxygen gas was introduced at a flow rate of 30 sccm and the plasma was triggered by a 1000 W radio frequency. Using a pulsed voltage of −20 kV, a pulse width of 100 μs and a pulsing frequency of 50 Hz, oxygen PIII was conducted for 3 h.

2.2. Surface characterization

X-ray photoelectron spectroscopy (XPS; Physical Electronics PHI 5802) with Al K_α irradiation was used to determine the chemical states and acquire the elemental depth profiles before and after PIII&D. The sputtering rate was estimated to be about 5.8 nm min^{-1}, based on similar sputtering experiments conducted on a SiO_2 reference. Static water contact angle measurements were performed by the sessile drop method on a Ramé-Hart (USA) instrument at ambient humidity and temperature to determine the surface hydrophilicity. Five-microliter water droplets were laid on the sample surface and the image of the droplet was immediately captured to calculate the contact angle. Each data point represents the average and standard deviation of five measurements conducted on different areas of each specimen for statistical analyses. Atomic force microscopy (AFM) using a Park Scientific Instruments/Auto Probe CP was employed to evaluate the surface morphology before and after ion implantation. The AFM images were obtained using the contact mode, and the root-mean-square roughness was determined by averaging the results obtained from three different areas.

2.3. Corrosion behavior

Weight loss measurements are often used to evaluate the corrosion rate of magnesium alloys. The samples with a surface area of 10×10 mm^2 were exposed to simulated body fluid (SBF) at pH 7.40 (ion concentrations (mM) of Na^+ 142.0, K^+ 5.0, Mg^{2+} 1.5, Ca^{2+} 2.5, Cl^- 147.8, HCO_3^- 4.2, $HPO_4^{2}-$ 1.0 and SO_4^{2-} 0.5) [26] at 37 °C for 1 and 3 days. The corrosion products formed on the sample surfaces during corrosion were removed by immersing the samples in chromic acid (200 g l^{-1} CrO_3 +10 g l^{-1} $AgNO_3$) for 5 min. Afterwards, the samples were rinsed in distilled water and alcohol, and dried overnight prior to the measurement.

The electrochemical tests are used to determine corrosion mechanism of magnesium alloy. The measurement was performed on a Zahner Zennium electrochemical workstation using the three-electrode technique. The potential was referenced to a saturated calomel electrode (SCE) and a platinum sheet served as the counter electrode. The test milieu was SBF, tryptic soy broth (TSB; Bacto) and complete cell culture medium consisting of a mixture of Dulbecco's modified Eagle's medium (DMEM; Gibco) and 10% fetal bovine serum (FBS; Gibco). The samples, with a surface area of 10×10 mm^2, were exposed to the solution at 37 °C. Electrochemical impedance spectroscopy (EIS) measurement was carried out after stabilization in the solution for 5 min. The data were recorded from 100 kHz to 100 mHz, with a 5 mV sinusoidal perturbing signal at the open-circuit potential. The polarization curves were acquired by scanning the potential at a rate of 1 mV s^{-1} from −300 to +600 mV following the EIS measurement.

Among the SBF, TSB and cell culture medium (DMEM+10% FBS), the cell culture medium is the closest to the physiological environment and was therefore used as the immersion solution to further evaluate the corrosion resistance of the ion implanted magnesium alloys. After immersion for 3 days in the cell culture medium at 37 °C, the samples were removed from the solution, rinsed with distilled water and dried in air. The surface morphology and microstructure were characterized by scanning electron microscopy (JEOL JSM-820 with an energy-dispersive spectroscopy (EDS) attachment).

2.4. Indirect cell viability and cell proliferation evaluation

Mouse MC3T3-E1 pre-osteoblasts were used in the in vitro cell culture experiments. They were cultured in DMEM supplemented with 10% FBS, 100 U ml^{-1} penicillin and 100 μg ml^{-1} streptomycin at 37 °C in a humidified atmosphere with 5% CO_2. Prior to the experiments, all the samples were sterilized by 70 vol.% ethanol for 30 min and rinsed three times with sterile phosphate-buffered saline (PBS).

The cell viability was evaluated by extract assay. The extracts were prepared with a sample surface area to extraction medium (DMEM) ratio of 1 ml cm^{-2} in a humidified atmosphere with 5% CO_2 at 37 °C for 3 days. The supernatant fluid was withdrawn and stored at 4 °C prior to the cytotoxicity test. The cells were cultured on a 96-well tissue culture plate at a density of 5000 cells

per well for 1 day to allow attachment. The medium was then replaced by 100 μl of extracts supplemented with 10% FBS. After incubation for 72 h, the extracts were replaced by the fresh medium [27] and 10 μl of (3-(4,5-dimethylthiazol-2-yl)-2,5-diphenyltetrazolium bromide was added to each well. After incubation for 4 h, formazen was formed and was dissolved by dimethyl sulfoxide. The absorbance was determined at 570 nm referenced to 630 nm on a microplate spectrophotometer (Biotek, USA).

Cell proliferation was evaluated using the BrdU incorporation ELISA kit (Roche, US). The test was performed according to an indirect method in which the extract collection and cell culture were conducted using the same protocol as the cell viability test. After 1 and 3 days, the cells were labeled with the fresh BrdU labeling medium for 4 h. Afterwards, the cells were fixed for 30 min at room temperature and incubated with the anti-BrdU-POD working solution for 2 h. The substrate solution was applied after rinsing several times with PBS. The reaction was stopped by 1 M H_2SO_4 and the absorbance was recorded at a wavelength of 450 nm on the microplate spectrophotometer.

2.5. Direct cell adhesion

The cells were seeded on each sample in 24-well tissue culture plates at a density of 5×10^4 cells per well and cultured for 5 h. The seeded samples were then rinsed twice with sterile PBS and fixed with 2% polyoxymethylene. The cytoskeleton protein F-actin was stained with phalloidin–fluorescein isothiocyanate (Sigma) and the nuclei were counterstained with Hoechst 33342 (Sigma). The cell images were captured by a fluorescence microscope (Carl Zeiss Axioplan 2).

2.6. Antimicrobial assay

Staphylococcus aureus bacteria were used to investigate the antimicrobial properties of the implanted binary magnesium alloys. Before the test, all implanted and unimplanted samples were sterilized in 70% ethanol for 30 min and rinsed with a 0.85% NaCl solution. TSB containing 10^7 *S. aureus* was incubated on the sample at 37 °C for 30 min. The suspended and non-adhered bacteria were then removed by rinsing in a NaCl solution and a LIVE/DEAD BacLight Viability Kit (Invitrogen) was used to stain the bacteria. Pictures of the bacteria were obtained at random on a fluorescence microscope with a green filter (excitation/emission, 420–480 nm/520–580 nm) and a red filter (excitation/emission, 480–550 nm/590–800 nm).

2.7. Statistical analysis

All the biological experiments were performed independently at least in triplicate, and three replicates were tested for each experimental point. The data were expressed as means ± standard deviation. The statistical analysis was based on one-way analysis of variance, and a p value of less than 0.05 was considered to be statistically significant.

3. Results

3.1. Materials characterization

The XPS depth profiles and high-resolution Zr3*d*, Mg1*s* and O1*s* spectra obtained from the Zr-implanted and Zr–O-implanted Mg–Ca and Mg–Sr alloys are depicted in Figs. 1–4. As shown in Fig. 1, a Zr-containing layer about 63 nm thick is formed on the Mg–Ca alloy surface after ion implantation and the Zr depth profile shows a Gaussian shape. This gradual structural change to the interface can effectively reduce the effects caused by the mismatch in the mechanical properties between the implanted metal and the magnesium alloy substrate. The high-resolution XPS spectra reveal that the valence states of magnesium and zirconium gradually change from the oxidized (Mg^{2+}, Zr^{2+}) to the metallic ones (Mg^0, Zr^0), accompanied by a gradually declining O1*s* intensity upon sputtering. Since no oxygen PIII is conducted here, the source of oxygen stems from the non-ultrahigh vacuum chamber in the plasma instrument [28].

In comparison with the Zr-implanted Mg–Ca, a higher relative content of oxygen is observed from the Zr–O-implanted Mg–Ca. Zirconium exhibits a more even distribution with a maximum concentration of about 20 at.% and the implantation depth increases from about 63 to 75 nm. Following the analysis of Fig. 1, the shift in the Zr3*d* and Mg1*s* peaks upon sputtering indicates that the near surface of the implanted sample is oxidized and a thicker oxide layer of about 75 nm, composed mainly of ZrO_2 and MgO, is formed on the Zr–O-implanted Mg–Ca. With regard to the Zr-implanted and Zr–O-implanted Mg–Sr (Figs. 3 and 4), the elemental chemical state changes with depth can also be analyzed using the method described above. It is found that the chemical state changes of magnesium and zirconium with depth follow trends similar to those in the ion implanted Mg–Ca.

AFM images representing a scanned range of 1 μm × 1 μm are shown in Fig. 5. The surface morphology is obviously altered by the plasma treatment. There are many large bud-like protrusions on the Zr-implanted and Zr–O-implanted surfaces. The protrusions on the Zr–O-implanted surface are more convex. Nevertheless, the implanted surface is still relatively uniform and dense. Observable variations in surface roughness can be found between the implanted surface and the unimplanted control. The surface roughness values increase from 4.67 nm (unimplanted) to 5.34 nm (Zr-implanted) and 9.42 nm (Zr–O-implanted) on the Mg–Ca alloy. Similarly, the surface roughness values increase from 2.16 nm (unimplanted) to 4.61 nm (Zr-implanted) and 7.29 nm (Zr–O-implanted) on the Mg–Sr alloy. The results provide experimental evidence that ion implantation is a suitable technique to produce a rough but uniform surface on magnesium.

Fig. 6 shows the contact angles measured from the implanted magnesium samples. The contact angles on the Zr-implanted and Zr–O-implanted magnesium alloy are much larger than those on the unimplanted control, implying that the implanted surfaces are more hydrophobic as a result of lower surface energy.

3.2. Corrosion behavior

Fig. 7 shows the weight losses after immersion in SBF. The average weight losses derived from the graph follow the following order: unimplanted > Zr-implanted > Zr–O-implanted. The weight losses measured from the Zr–O-implanted Mg–Ca and Mg–Sr are significantly lower than those from the unimplanted ones at every time point. With regard to the Mg–Sr alloy, the weight loss from the Zr–O-implanted sample is also significantly lower than that from the Zr-implanted one, thus revealing that dual zirconium and oxygen ion implantation significantly decreases the degradation rate of the Mg–Ca and Mg–Sr alloys.

Figs. 8 and 9 exhibit the potentiodynamic polarization curves of the Mg–Ca and Mg–Sr alloys before and after implantation in the SBF, TSB and cell culture medium, respectively. The cathodic polarization curve is considered to represent the cathodic hydrogen evolution through water reduction, while the anodic one represents dissolution of magnesium. The corrosion potential and corrosion current density can be derived directly from the region in the cathodic polarization curves by Tafel region extrapolation. Table 1 presents the corrosion potential and corrosion current density deduced from Figs. 8 and 9. The unimplanted sample has a fairly

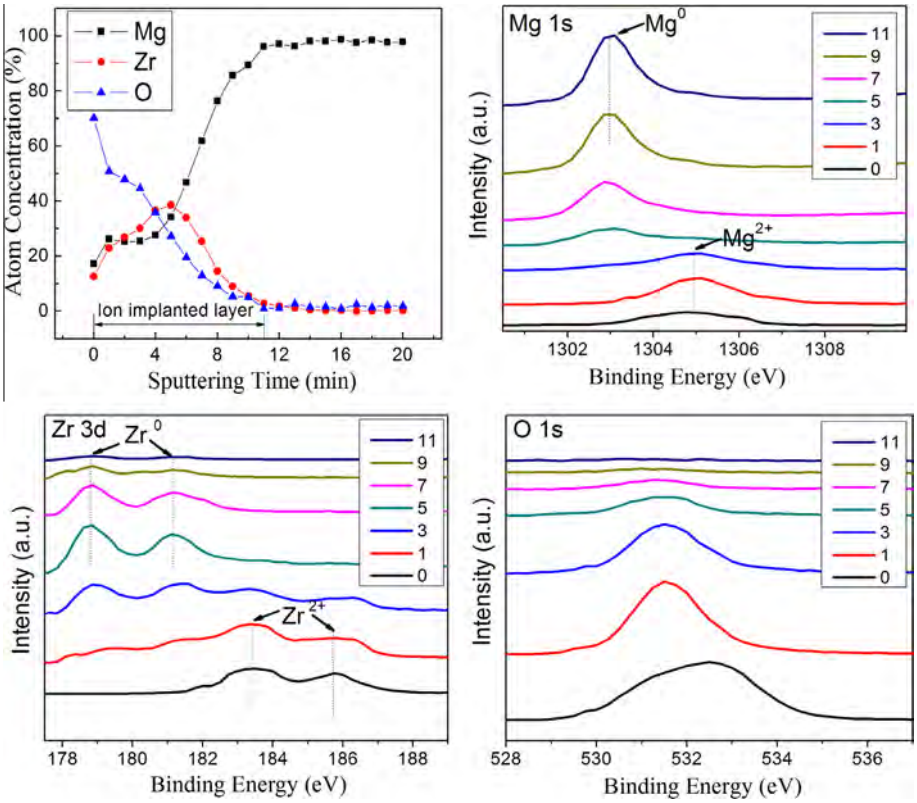

Fig. 1. XPS depth profile and high-resolution XPS Mg1*s*, Zr3*d* and O1*s* spectra acquired from Zr-implanted Mg–Ca at different sputtering times, with the numbers in the figures denoting the sputtering time. The ion implanted layer depth is about 63 nm.

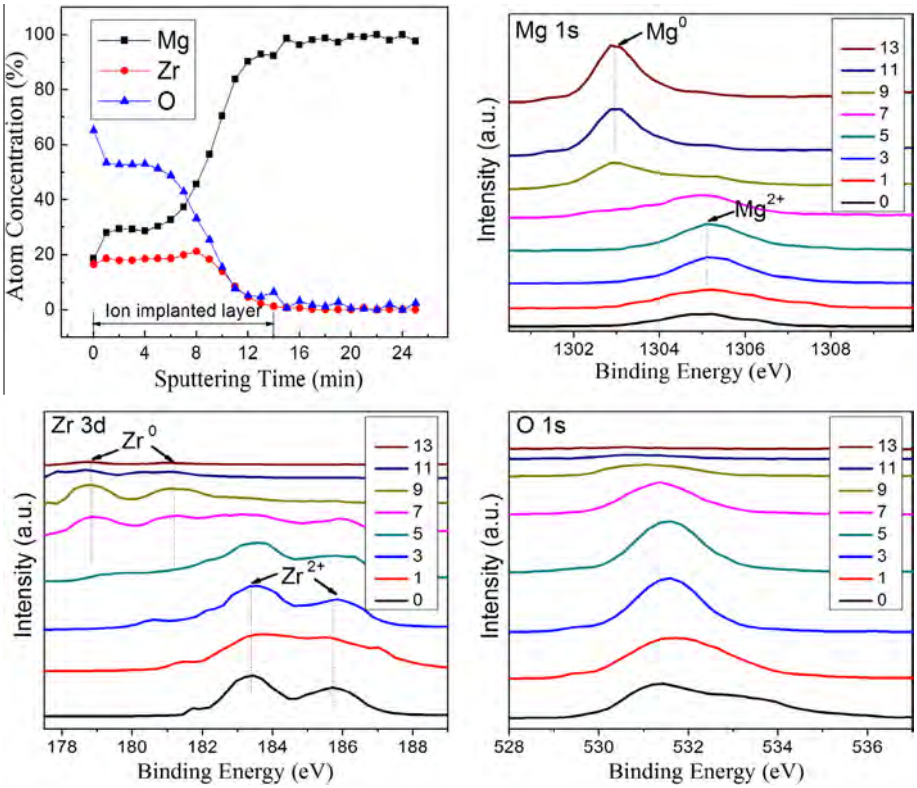

Fig. 2. XPS depth profile and high-resolution XPS Mg1*s*, Zr3*d* and O1*s* spectra acquired from Zr–O-implanted Mg–Ca at different sputtering times, with the numbers in the figures denoting the sputtering time. The ion implanted layer depth is about 75 nm.

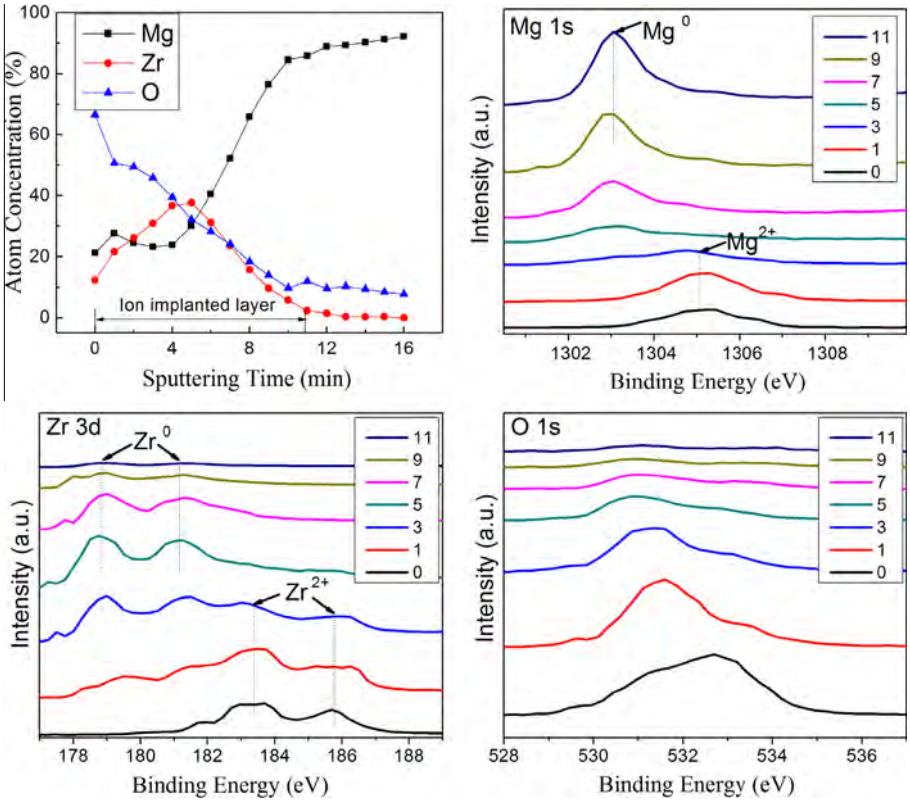

Fig. 3. XPS depth profile and high-resolution XPS Mg1*s*, Zr3*d* and O1*s* spectra acquired from Zr-implanted Mg–Sr at different sputtering times, with the numbers in the figures denoting the sputtering time. The ion implanted layer depth is about 63 nm.

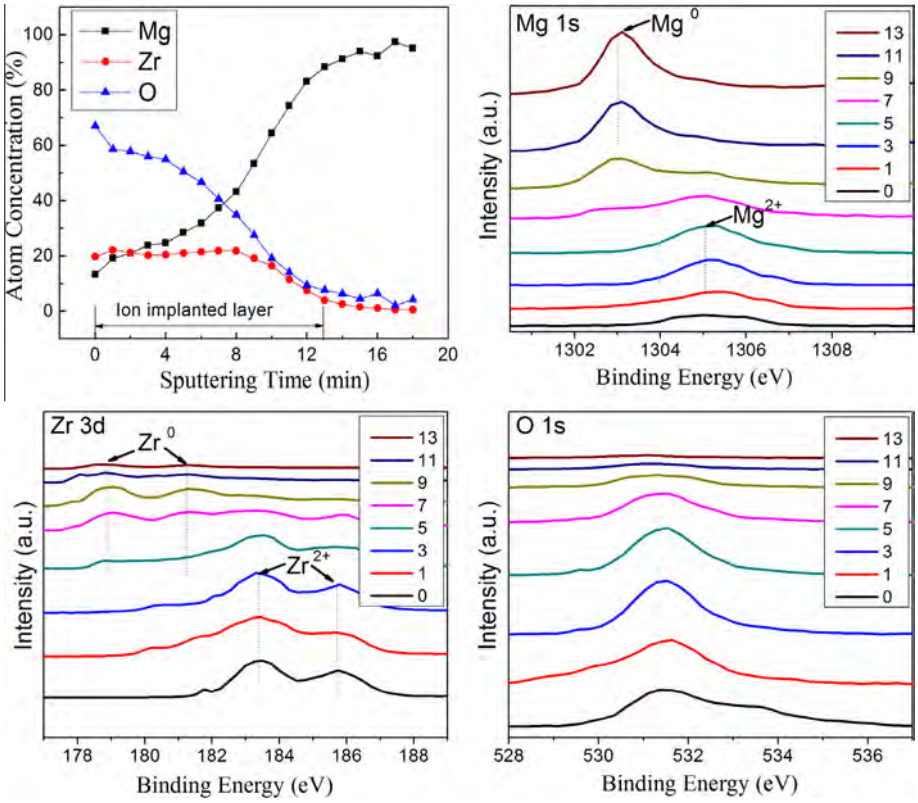

Fig. 4. XPS depth profile and high-resolution XPS Mg1*s*, Zr3*d* and O1*s* spectra acquired from Zr–O-implanted Mg–Sr at different sputtering times, with the numbers in the figures denoting the sputtering time. The ion implanted layer depth is about 75 nm.

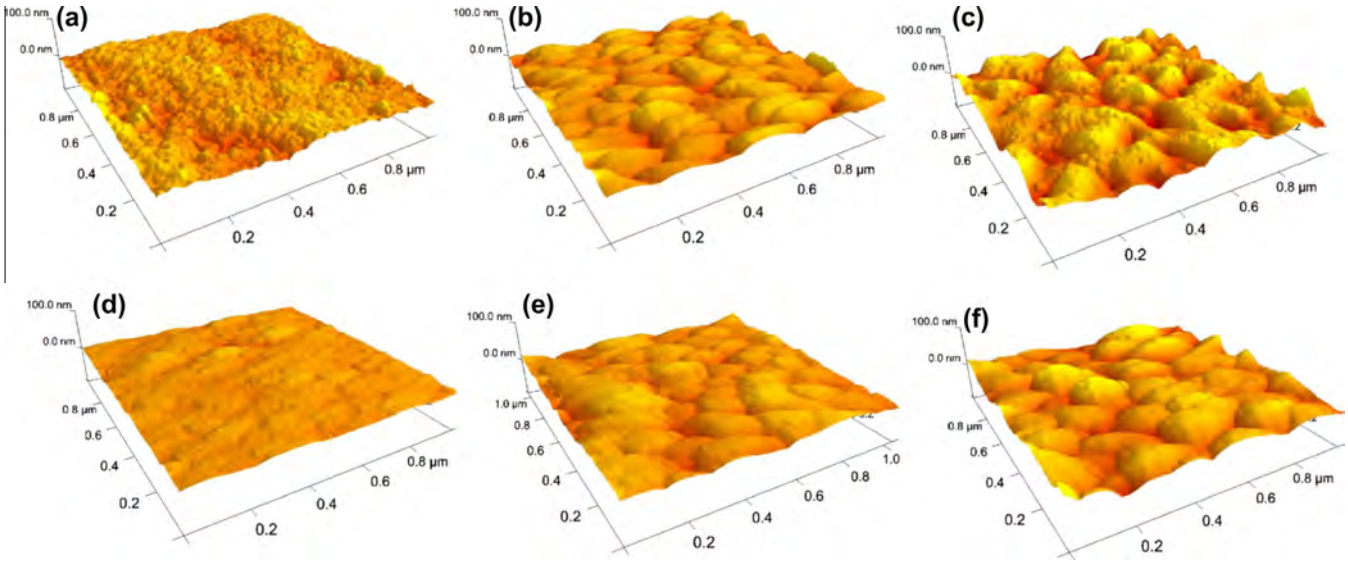

Fig. 5. AFM images of (a) unimplanted Mg–Ca, (b) Zr-implanted Mg–Ca, (c) Zr–O-implanted Mg–Ca, (d) unimplanted Mg–Sr, (e) Zr-implanted Mg–Sr and (f) Zr–O-implanted Mg–Sr.

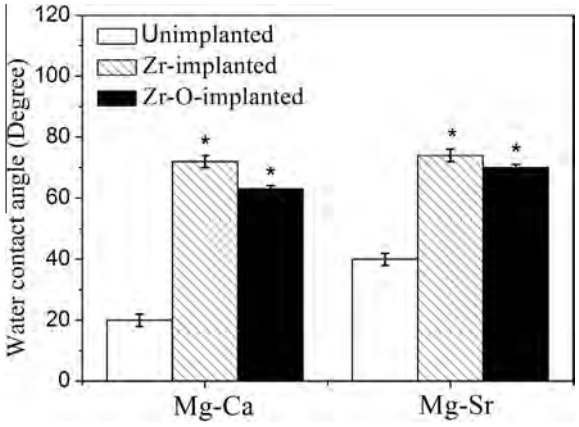

Fig. 6. Water contact angles measured on unimplanted, Zr-implanted and Zr–O-implanted Mg–Ca and Mg–Sr samples, with the statistical significance indicated by * referring to $p < 0.01$.

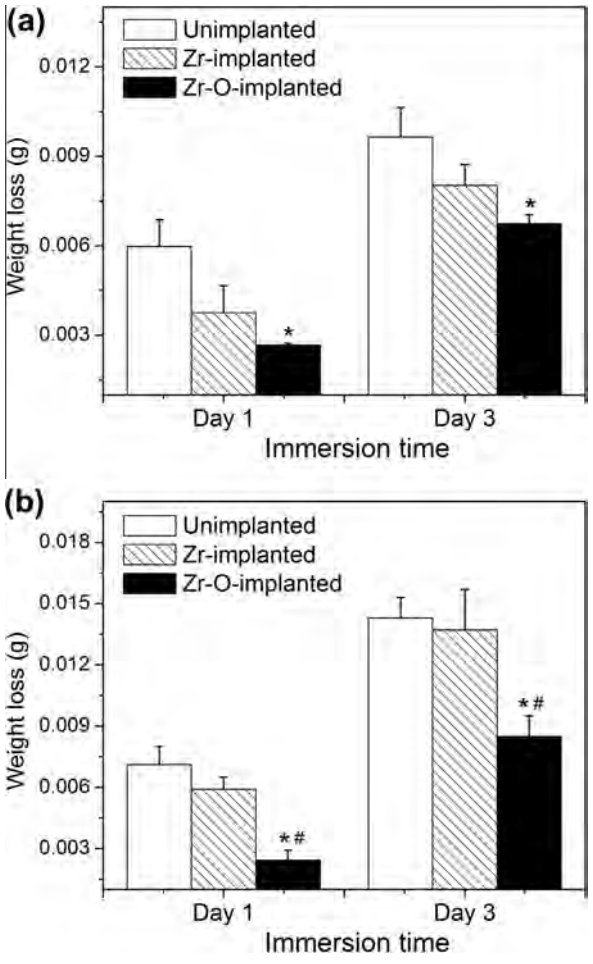

Fig. 7. Weight losses measured from the unimplanted, Zr-implanted and Zr–O-implanted (a) Mg–Ca and (b) Mg–Sr samples after immersion in SBF for 1 and 3 days. Statistically significant differences at $^{*}p < 0.05$ compared to the unimplanted control and $^{\#}p < 0.05$ compared to the Zr implanted sample.

negative corrosion potential and, after ion implantation, the corrosion potential shifts toward a nobler direction. The corrosion current densities measured from the unimplanted, Zr-implanted and Zr–O-implanted Mg–Ca and Mg–Sr exhibit descent trends not only in the SBF but also in the TSB and cell culture medium. This suggests that dual zirconium and oxygen ion implantation appreciably diminishes the electrochemical degradation rate.

The representative EIS spectra (Nyquist plots) acquired from the unimplanted, Zr-implanted and Zr–O-implanted Mg–Ca and Mg–Sr after immersion in SBF, TSB and cell culture medium for 5 min are presented in Figs. 8 and 9. The capacitive arc at high frequencies results from charge transfer whereas those at medium or low frequencies results from the effects of the surface film. Regardless of the medium, the capacitive arcs are clearly enlarged after ion implantation. In particular, the diameter of the capacitive arc observed from the Zr–O-implanted Mg–Ca and Mg–Sr samples is more than five times that of the unimplanted control. Moreover, an inductive arc is visible in the low frequency region. The inductive arc is usually related to the formation, adsorption and desorption of corrosion products on the surface. It is known that a larger diameter arc represents better corrosion resistance, hence the EIS

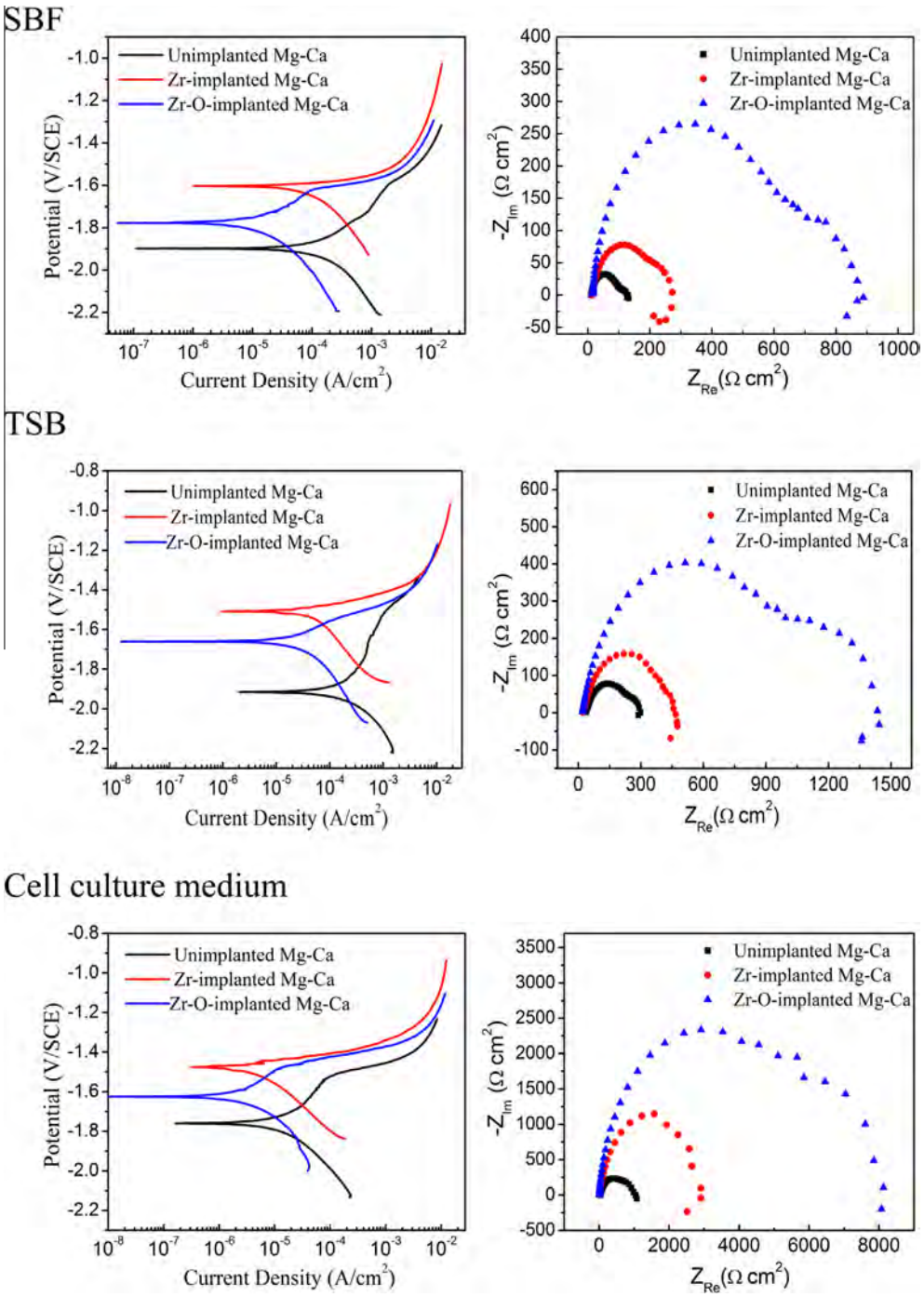

Fig. 8. Polarization curves and EIS spectra of unimplanted, Zr-implanted and Zr–O-implanted Mg–Ca in SBF, TSB and cell culture medium.

results indicate that dual zirconium and oxygen ion implantation appreciably improves the corrosion resistance of Mg–Ca and Mg–Sr alloys.

Fig. 10 displays the corroded morphology of the unimplanted, Zr-implanted and Zr–O-implanted Mg–Ca and Mg–Sr alloys after immersion in the cell culture medium for 3 days. General corrosion is observed from the surface of the unimplanted Mg–Ca and Mg–Sr alloys, as manifested by homogeneously distributed corrosion products and networks of cracks (Fig. 10a and d). EDS (inset in Fig. 10a) shows that the corrosion products are rich in Mg, O, Ca and P, and may be due to the precipitation of MgO and/or $Mg(OH)_2$, phosphates and carbonates during immersion [14]. In comparison with the unimplanted Mg–Ca and Mg–Sr, most areas on the Zr-implanted surface are smooth, without serious corrosion attack (Fig. 10b and e). Only some microcracks and white precipitates composed of Mg, Ca, etc. (EDS inset in Fig. 10e) are visible from the local area. Among all the samples, Zr–O-implanted Mg–Ca and Mg–Sr alloy degrade slowly, showing only a few microcracks on the sample surfaces (Fig. 10c and f) and the smallest degree of corrosion.

3.3. Indirect cell viability and cell proliferation evaluation

Fig. 11 shows the cell viability of the unimplanted, Zr-implanted and Zr–O-implanted Mg–Ca and Mg–Sr samples for 72 h. The cells

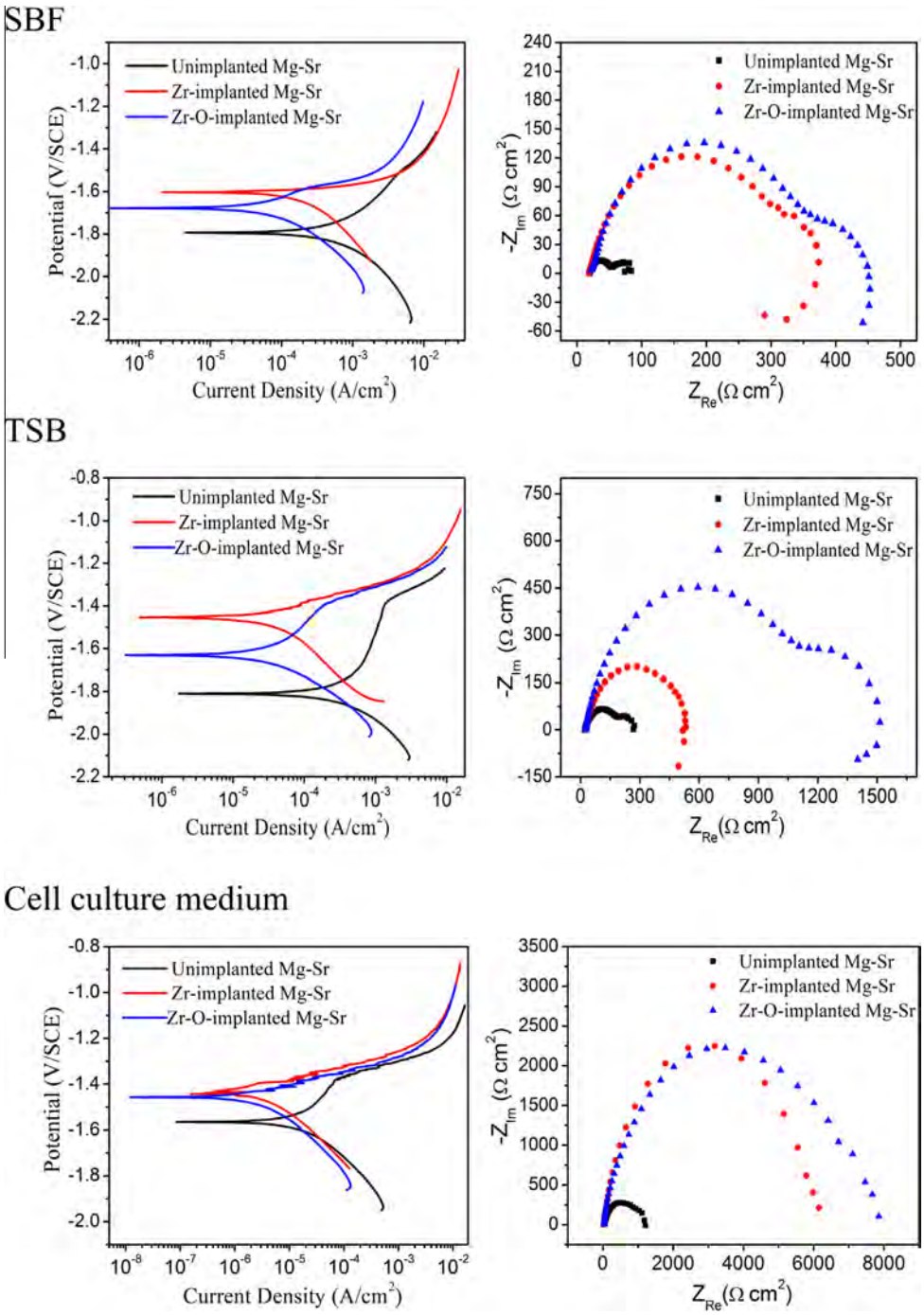

Fig. 9. Polarization curves and EIS spectra of unimplanted, Zr-implanted and Zr–O-implanted Mg–Sr in SBF, TSB and cell culture medium.

cultured in the extract medium of the unimplanted Mg–Ca and Mg–Sr alloy samples show lower cell viability than the Zr-implanted and Zr–O-implanted samples, revealing improved cytocompatibility after surface treatment.

The fold change of BrdU incorporation after 1 and 3 days is illustrated as a histogram in Fig. 12. Significantly increased BrdU incorporation is observed from the Zr-implanted Mg–Sr and Zr–O-implanted Mg–Ca and Mg–Sr alloy samples throughout the culturing period compared to the unimplanted control, suggesting that the cell proliferation rate is significantly improved after surface treatment. Since high osteoblast proliferation probably leads to a larger mass of bone tissues around the implant, more robust bone–implant bonding is expected in vivo and more work is being conducted for corroboration.

3.4. Direct cell adhesion

Fig. 13 depicts the morphology of the mouse MC3T3-E1 pre-osteoblasts on the binary magnesium alloy after culturing for 5 h, revealing focal adhesion and cell spreading. Most of the MC3T3-E1 pre-osteoblasts on the unimplanted sample fail to spread well, although they appear to attach to the sample surface. In contrast, the Zr-implanted and Zr–O-implanted samples show enhanced organized F-actin. In particular, on the Zr–O-implanted

Table 1
i_{corr} and E_{corr} values determined from the polarization curves.

Solution	Sample	i_{corr} (A cm^{-2})	E_{corr} (V/SCE)
SBF	Unimplanted Mg–Ca	2.3×10^{-4}	−1.92
	Zr-implanted Mg–Ca	1.2×10^{-4}	−1.60
	Zr–O-implanted Mg–Ca	2.6×10^{-5}	−1.78
	Unimplanted Mg–Sr	1.0×10^{-3}	−1.79
	Zr-implanted Mg–Sr	2.5×10^{-4}	−1.60
	Zr–O-implanted Mg–Sr	1.7×10^{-4}	−1.68
TSB	Unimplanted Mg–Ca	2.8×10^{-4}	−1.91
	Zr-implaned Mg–Ca	4.9×10^{-5}	−1.51
	Zr–O-implanted Mg–Ca	4.1×10^{-5}	−1.66
	Unimplanted Mg–Sr	4.3×10^{-4}	−1.81
	Zr-implanted Mg–Sr	4.2×10^{-5}	−1.45
	Zr–O-implanted Mg–Sr	4.0×10^{-5}	−1.63
Cell culture medium	Unimplanted Mg–Ca	1.5×10^{-5}	−1.76
	Zr-implaned Mg–Ca	6.4×10^{-6}	−1.48
	Zr–O-implanted Mg–Ca	4.6×10^{-6}	−1.63
	Unimplanted Mg–Sr	2.3×10^{-5}	−1.56
	Zr-implanted Mg–Sr	5.0×10^{-6}	−1.44
	Zr–O-implanted Mg–Sr	4.0×10^{-6}	−1.45

samples, the attached cells exhibit more obvious filopodia and flattened membranes, suggesting that better cytocompatibility is accomplished on the Zr–O-implanted binary magnesium alloy.

3.5. Antimicrobial properties

Fig. 14 displays the morphology of adhered bacteria on the unimplanted, Zr-implanted and Zr–O-implanted samples observed by fluorescent microscopy. Live bacteria are stained in green, whereas dead bacteria manifest in red. The results suggest that the numbers of live bacteria on the Zr–O-implanted and Zr-implanted samples are remarkable smaller than that on the unimplanted control. In addition, small dead bacteria can be found on the implanted sample (Fig. 14f).

4. Discussion

4.1. Improved corrosion resistance on the plasma-modified binary magnesium

The impedance measurement results are in agreement with those obtained from the polarization test. They both show that dual zirconium and oxygen ion implantation dramatically improves the corrosion resistance of Mg–Ca and Mg–Sr alloys. In order to explain the EIS spectra, according to the physical structure of the electrode, two equivalent circuits presented in Fig. 15 are proposed to fit the Nyquist plots. Fig. 15a is used to fit the curves without the inductive arc and Fig. 15b shows the fit with the inductive arc. Here, R_s is the solution resistance between the reference electrode and working electrode. A constant phase element, CPE_f, represents the surface film capacitance and R_f is the relevant resistance of the surface film. R_{pore} is the sum of the resistances of all the pores in the surface film. Another constant phase element, CPE_{dl}, represents the capacitance of the double layer and R_t is the charge transfer resistance related to the electrochemical reaction. The CPE_{dl} (or CPE_f) value is defined by two values, $Y0_{dl}$ (or $Y0_f$) and n_{dl} (or n_f), where $Y0_{dl}$ (or $Y0_f$) is the admittance constant of the CPE_{dl} (or CPE_f), n_{dl} and n_f are indices of the dispersion effects of CPE_{dl} and CPE_f, respectively, and represent deviations from the ideal capacitance due to the inhomogeneity and roughness of the electrode on the micro scale [29]. The value of n is always in the range $0 < n \leqslant 1$. If n is equal to 1, CPE_{dl} (or CPE_f) is identical to that of a capacitor. In addition, L denotes the inductance and R_L represents the corresponding resistance. The fitted results are listed in Tables 2 and 3. The results show that R_t and R_f (or R_{pore}) increase while $Y0_{dl}$ and $Y0_f$ decrease after ion implantation. In particular, the Zr–O-implanted sample shows the largest R_t and R_f and the smallest $Y0_{dl}$ and $Y0_f$. Larger R_f and R_t suggest the formation of a more compact corrosion product layer on the sample surface and higher resistance to magnesium dissolution, whereas smaller $Y0_{dl}$ and $Y0_f$ correspond to higher values of R_t and R_f, respectively, in the experiment, indicating that there is greater corrosion stability

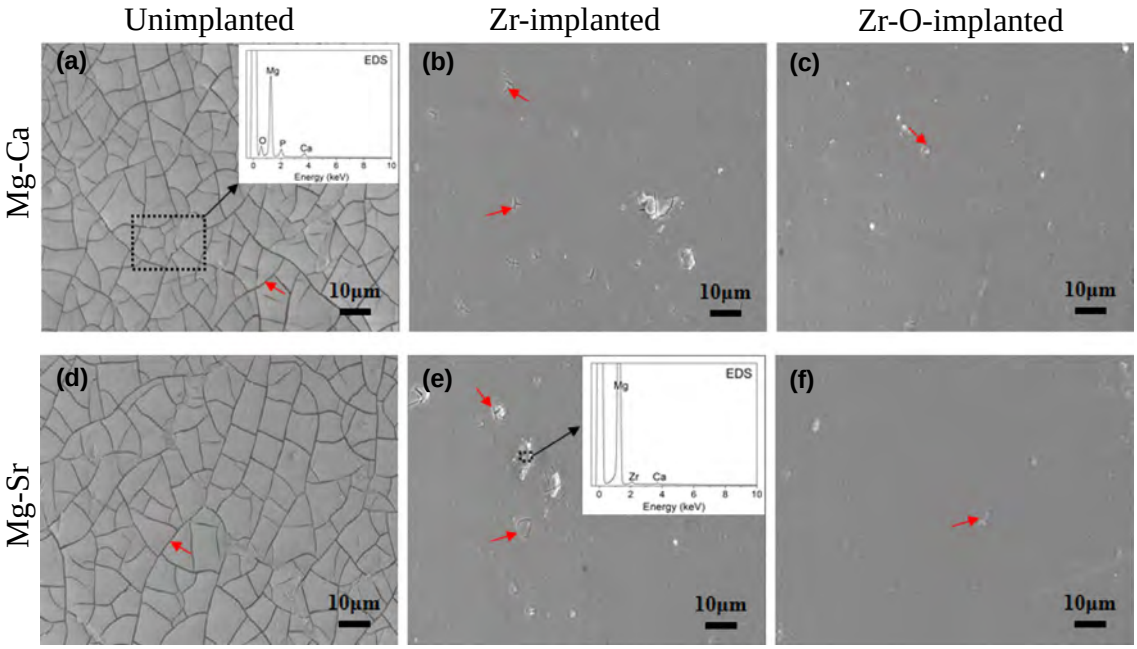

Fig. 10. Surface morphologies of (a) unimplanted Mg–Ca, (b) Zr-implanted Mg–Ca, (c) Zr–O-implanted Mg–Ca, (d) unimplanted Mg–Sr, (e) Zr implanted Mg–Sr and (f) Zr–O-implanted Mg–Sr alloy samples after immersion for 3 days in the cell culture medium, with small red arrows representing cracks. The inset shows the EDS result of a typical corroded area.

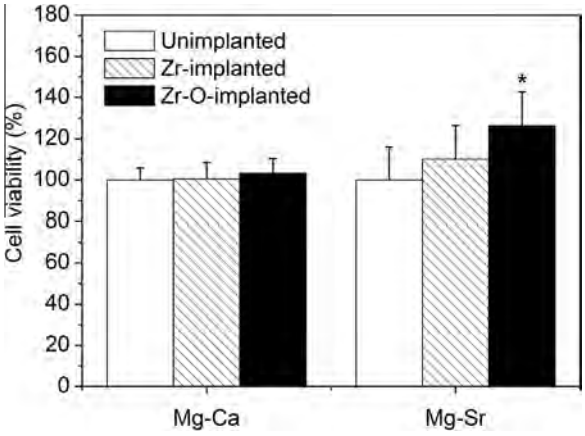

Fig. 11. Cell viability of MC3T3-E1 pre-osteoblasts cultured in different extracts supplemented with 10% FBS. The absorbance is monitored at a wavelength of 570 nm referenced to 640 nm to determine the cell viability in comparison with the unimplanted control. Statistically significant differences at $^{*}p < 0.05$ vs. control.

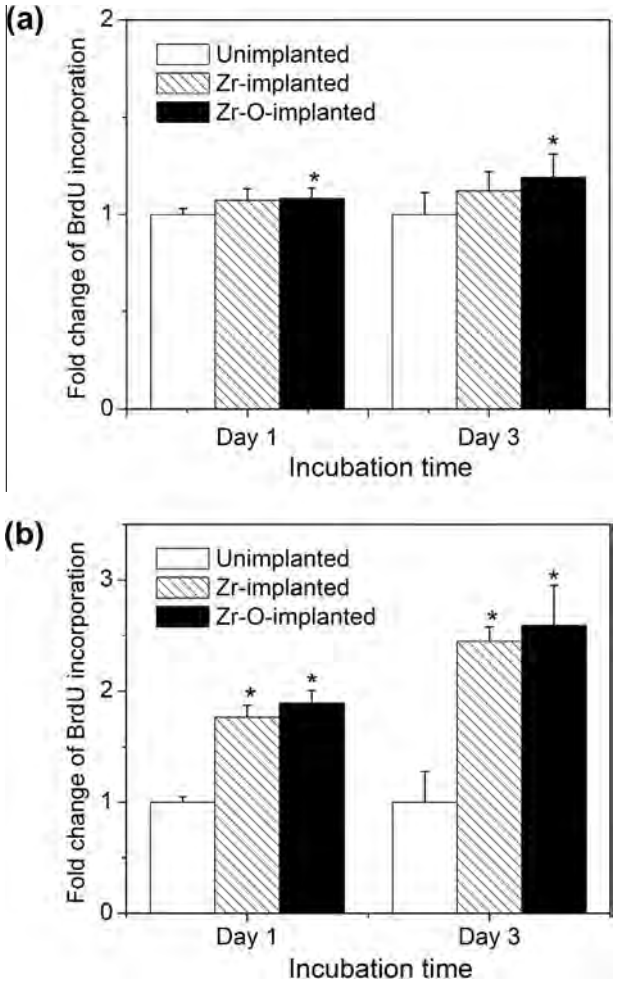

Fig. 12. Cell proliferation evaluated by the fold change of the incorporation of BrdU on the unimplanted, Zr-implanted and Zr–O-implanted binary magnesium alloys after 1 and 3 days. The data are normalized to the unimplanted control: (a) Mg–Ca alloy and (b) Mg–Sr alloy. Statistically significant differences at $^{*}p < 0.05$ vs. control.

after ion implantation [30]. These results show that ion implantation retards surface corrosion on the Mg–Ca and Mg–Sr alloys and, in particular, dual zirconium and oxygen ion implantation markedly improves the corrosion resistance. The results are in agreement with the weight losses determined from the immersion tests. Here, the impedance in the cell culture medium is much higher than that in the SBF and TSB, and this may be attributed to the albumin in the cell culture medium forming a corrosion-blocking layer on magnesium [31].

Improvement in the corrosion resistance may be related to the formation of the corrosion-resistant metal oxide and dramatically reduced magnesium content in the near surface. In our process, the surface composition of the magnesium alloy is altered by metal ion implantation and subsequent O PIII. Metal ion implantation produces a thick Zr-containing modified layer. Because of the retardation effect of zirconium, diffusion of magnesium atoms from the substrate to the surface is restricted and the magnesium content in the near surface is dramatically reduced. Reduction in the amount of reactive magnesium may enhance the corrosion resistance [15]. On the other hand, the corrosion- resistant metal oxide plays a role in the improved corrosion resistance. In our experiments, after metal ion implantation, O PIII is further conducted to modify the surface. Under high-energy bombardment, oxygen ions penetrate the surface and react with zirconium and magnesium simultaneously. The process finally results in the formation of a protective ZrO_2-containing oxide film. This surface oxide is more stable in the SBF, TSB and cell culture medium than that on the Zr-implanted and unimplanted samples according to our electrochemical and immersion tests.

4.2. Antimicrobial properties of plasma-modified binary magnesium alloys

Microbial infection frequently threatens the health of patients and has become the predominant cause of biomaterials failures [32]. In order to reduce the chance of postsurgical infection, the development of biomedical implants with effective antimicrobial properties is imperative. Although antibacterial coatings have been researched extensively, it is still a challenge to produce one with clinical potential on a magnesium alloy. To our knowledge, the use of ion implantation to improve the antibacterial properties of magnesium has seldom been reported.

It is well known that the early stage after surgery is critical to the prevention of bacterial infection. This is because, once bacteria have attached to and formed biofilms on the surface of biomaterials, it is very difficult to remove them, and this frequently results in implant failure and requires repeated surgery [33]. The current study shows remarkable differences in bacterial adhesion between the plasma-modified binary magnesium alloy and the unimplanted control. This is mainly due to the difference in the physicochemical characteristics, such as the surface chemical composition and surface hydrophobicity. Zirconium and zirconium oxide have been reported to have the ability to inhibit the level of bacterial colonization on the surface [23–25]. Hence, the introduction of zirconium and the formation of zirconium oxide appear to be possible reasons for the suppressed bacteria adhesion here. In addition, the ability of the plasma-modified surface to decrease bacterial adhesion can be attributed to the lower surface energy and surface hydrophobicity. Quirynen and Bollen [34] also found that increased surface energy fosters more bacterial adhesion. Our study shows that the bacteria have less affinity to the ZrO_2-containing magnesium alloy than to the unimplanted control. This is important for clinical applications as it reduces implant infection.

Our results indicate that the implanted surface can effectively kill bacteria even if some bacteria adhere to the surface. Although the exact mechanism of the antimicrobial action needs further study, it is surmised that it may be related to the surface charges on the sample and different electrode potentials between the implanted metal and the substrate. When the plasma-treated magnesium alloy is immersed in a physiological liquid, the surface-ionized

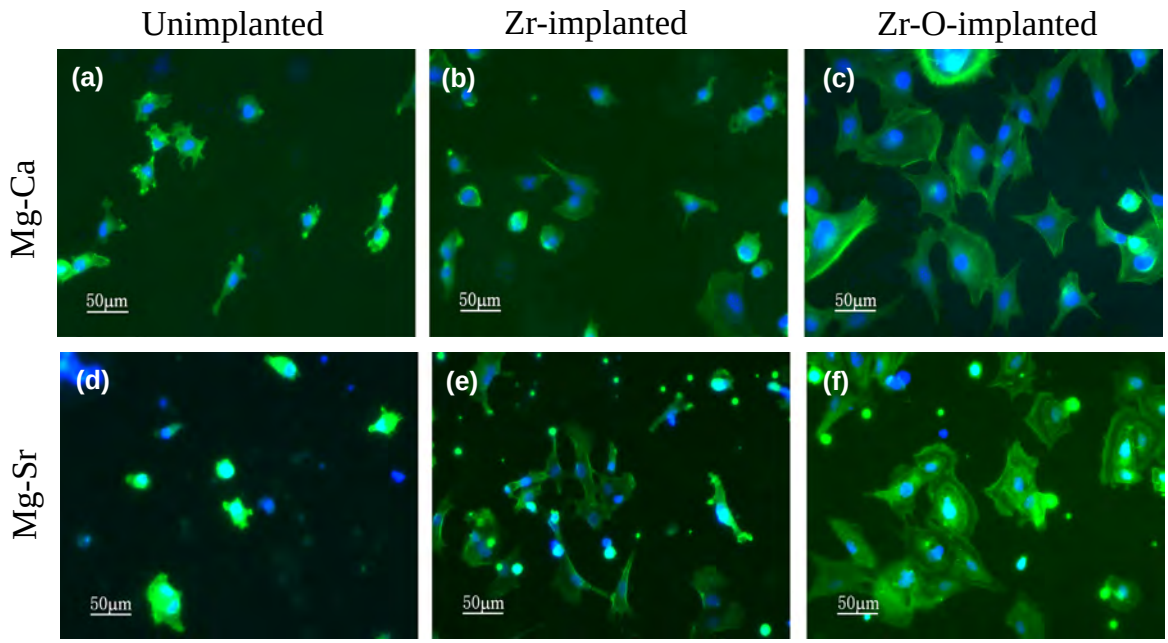

Fig. 13. Fluorescent images of MC3T3-E1 pre-osteoblasts after culturing for 5 h on (a) unimplanted Mg–Ca, (b) Zr-implanted Mg–Ca, (c) Zr–O-implanted Mg–Ca, (d) unimplanted Mg–Sr, (e) Zr implanted Mg–Sr and (f) Zr–O-implanted Mg–Sr alloy samples.

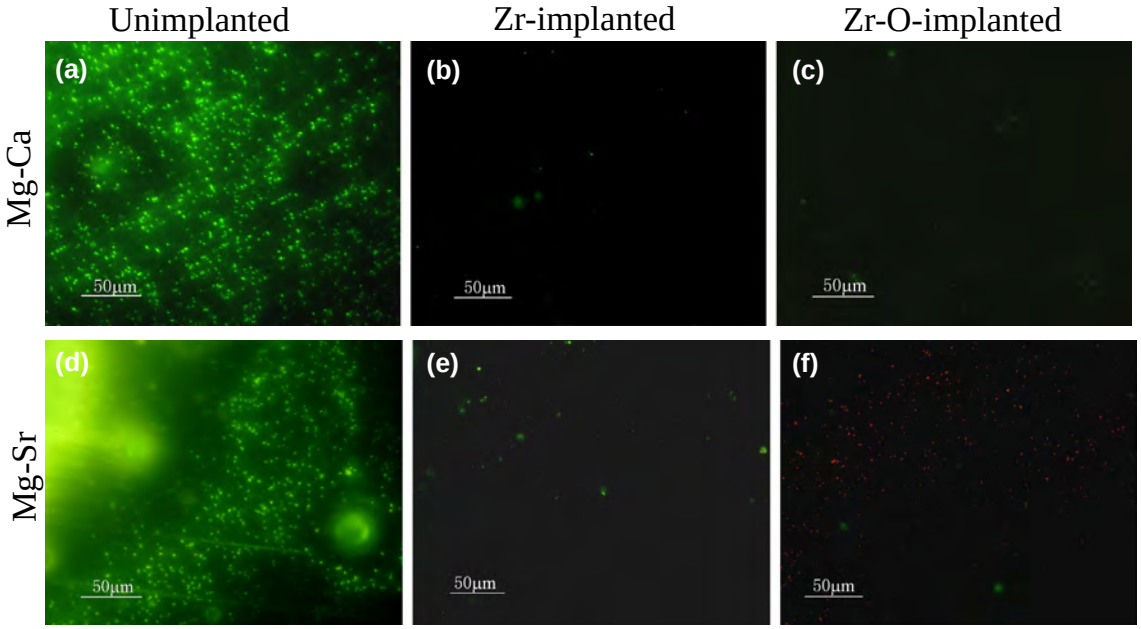

Fig. 14. Fluorescent microscopic views of magnesium samples after 30 min of bacteria culture: (a) unimplanted Mg–Ca, (b) Zr-implanted Mg–Ca, (c) Zr–O-implanted Mg–Ca, (d) unimplanted Mg–Sr, (e) Zr-implanted Mg–Sr and (f) Zr–O-implanted Mg–Sr.

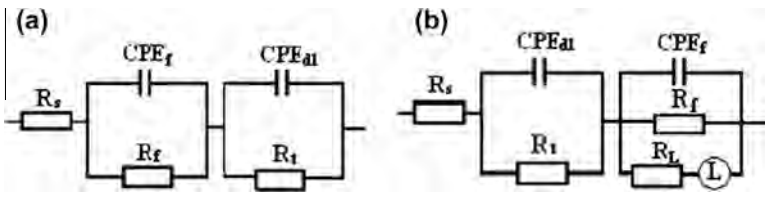

Fig. 15. Equivalent circuit for analysis of the EIS spectra of binary magnesium alloys immersed in the SBF and cell culture medium for (a) spectra without an inductive arc and (b) spectra with an inductive arc.

Table 2
Fitted EIS results of Mg–Ca alloy in SBF, TSB, and cell culture medium.

Solution	Sample	R_s (Ω cm^2)	$Y0_f$ (Ω^{-1} cm^{-2} s^{-n})	n_f	R_f or R_{pore} (Ω cm^2)	$Y0_{d1}$ (Ω^{-1} cm^{-2} s^{-n})	n_{dl}	R_t (Ω cm^2)
SBF	Unimplanted	10.5	4.96E-5	0.968	51.47	2.134E-3	0.5214	67.47
	Zr-implanted	11.43	4.414E-5	0.9153	127.9	1.265E-3	0.5399	195.9
	Zr–O-implanted	22.19	3.596E-6	0.9618	535.9	2.173E-4	0.7193	370.6
TSB	Unimplanted	35.05	3.175E-5	0.9043	121.1	8.054E-4	0.5142	161.3
	Zr-implanted	23.32	2.907E-5	0.9408	272.5	7.769E-4	0.5339	199.4
	Zr–O-implanted	18.73	4.85E-6	0.8972	777.8	2.368E-4	0.605	885.2
Cell culture medium	Unimplanted	16.53	7.645E-5	0.7069	19.58	1.089E-4	0.723	887.5
	Zr-implanted	13.98	7.957E-5	0.7203	963.3	3.645E-5	0.8706	2449
	Zr–O-implanted	13.23	3.417E-6	0.9367	2983	1.339E-5	0.9151	7835

Table 3
Fitted EIS results of Mg–Sr alloy in SBF, TSB, and cell culture medium.

Solution	Sample	R_s (Ω cm^2)	$Y0_f$ (Ω^{-1} cm^{-2} s^{-n})	n_f	R_f or R_{pore} (Ω cm^2)	$Y0_{d1}$ (Ω^{-1} cm^{-2} s^{-n})	n_{dl}	R_t (Ω cm^2)
SBF	Unimplanted	19.65	4.891E-3	0.8937	26.34	5.512E-5	0.8154	34.93
	Zr-implanted	17.96	1.1E-3	0.5206	175.7	2.076E-5	0.9133	223.4
	Zr–O-implanted	39.52	5.806E-4	0.4863	236.8	5.805E-6	0.952	233
TSB	Unimplanted	19.92	1.67E-3	0.4496	189.2	3.18E-5	0.8897	111.4
	Zr-implanted	23.54	7.75E-4	0.5573	207.7	3.246E-5	0.9477	346.7
	Zr–O-implanted	25.06	2.943E-4	0.6175	727	4.43E-6	0.8799	949.6
Cell culture medium	Unimplanted	20.66	6.889E-5	0.701	24.62	6.93E-5	0.6862	1089
	Zr-implanted	25.93	2.154E-5	0.8585	34.05	1.795E-5	0.8515	5960
	Zr–O-implanted	33.83	3.538E-6	0.9081	1174	6.743E-6	0.8365	5949

metals (Zr^{2+} and Mg^{2+}) with positive charges interact with the negatively charged microbial cell membranes. This may cause alternation of the cell permeability or disruption of the membrane integrity, ultimately resulting in the leakage of proteinaceous and other intracellular constituents [35]. In addition, metal ion implantation can trigger microgalvanic effects in the physiological environment. Since zirconium and magnesium have different standard electrode potentials, of −1.529 and −2.363 V, respectively, the proton-depleted regions produced by the microgalvanic coupling reactions can inactive ATP synthesis, ion transport and metabolite sequestration, ultimately leading to bacteria death [36].

4.3. Biocompatibility of plasma-modified binary magnesium alloys

The cytocompatibility of the biomaterials is another important issue. Although some modified surfaces can inhibit bacteria adhesion or kill bacteria, they may impose adverse effects on cell adhesion and growth. An ideal implantable antibacterial surface should not only be able to resist bacterial adhesion and its subsequent biofilm formation, but should also possess good biocompatibility. The cytocompatibility of biomaterials is closely related to the cells in contact with them, and particularly to cell adhesion onto their surface. The surface characteristics of the materials, such as surface chemistry, roughness and other topographic features, play an important role in pre-osteoblast adhesion. In our study, pre-osteoblasts attached and proliferated well on the Zr–O-implanted surface, and no cytotoxic effects could be observed from the MC3T3-E1 cells. This can be attributed to the formation of biocompatible ZrO_2, which offers a more favorable environment for cell growth. Moreover, the increased surface roughness after ion implantation is favorable to cell adhesion and proliferation.

On biodegradable magnesium alloys, the interface between the sample surface and surrounding medium is crucial to cell adhesion and growth. Rapid corrosion of magnesium results in hydrogen evolution, metal dissolution and local alkalization, and these processes produce deleterious and even fatal effects to surrounding cells [37,38]. In the present work, both cell adhesion and proliferation are significantly improved on the Zr–O-implanted binary magnesium alloys. The improved biological response to the modified magnesium alloy is believed to be related to the alloy's corrosion resistance, since normally the cytotoxicity of magnesium alloy is due to its high degradation rate, which gives rise to interface reaction between the unimplanted Mg–Ca (or Mg–Sr) and the corrosive medium, consequently adversely affecting cell adhesion and growth. After dual zirconium and oxygen ion implantation, the ZrO_2-containing surface layer serves as a barrier to retard corrosion, and only slight corrosion can be observed after immersion in the cell culture medium for 3 days (Fig. 10c and f). Reduction of the degradation rate of magnesium not only creates a relatively stable interface for cell adhesion and growth, but also reduces the release of corrosion products that can compromise the cytotoxicity [30].

It should be noted that the responses of bacteria and pre-osteoblasts are different according to this study: the adhesion of bacteria is impeded whereas that of osteoblasts is promoted. This difference is likely due to the difference in the structure and size between the bacterial cells and the pre-osteoblasts. The exact mechanism needs further study, and more work on this is currently being performed in our laboratory.

5. Conclusion

A ZrO_2-containing protective oxide layer is produced on biodegradable Mg–Ca and Mg–Sr alloys by dual zirconium and oxygen ion implantation. The plasma treatment enhances the corrosion resistance of the magnesium alloy appreciably in SBF, TSB and cell culture medium. The formation of biocompatible ZrO_2 in the near surface and the decreased degradation rate produce a relatively stable and biofriendly interface for cell attachment and growth, resulting in enhanced cytocompatibility in vitro. Dual zirconium and oxygen ion implantation additionally produces good antimicrobial properties. Our study suggests that biodegradable Mg–Ca

and Mg–Sr alloys with a plasma-modified surface show good potential as orthopedic implants.

Acknowledgements

This work was jointly supported by HKU Seed Funding for Basic Research, Hong Kong Research Grant Council General Research Fund #124009, #718913, #112510 and #112212, City University of Hong Kong Applied Research Grant (ARG) #9667066, an AOTRAUMA Research Startup Grant and the Shenzhen Key Laboratory for Innovative Technology in Orthopaedic Trauma, The University of Hong Kong Shenzhen Hospital.

Appendix A. Figures with essential color discrimination

Certain figures in this article, particularly Figs. 1–5, 8–10, 13 and 14, are difficult to interpret in black and white. The full color images can be found in the on-line version, at http://dx.doi.org/10.1016/j.actbio.2013.10.012.

References

[1] Witte F, Kaese V, Haferkamp H, Switzer E. In vivo corrosion of four magnesium alloys and the associated bone response. Biomaterials 2005;26:3557–63.
[2] Staiger MP, Pietak AM, Huadmai J, Dias G. Magnesium and its alloys as orthopedic biomaterials: a review. Biomaterials 2006;27:1728–34.
[3] Witte F, Fischer J, Nellesen J, Crostack H, Kaese V, Pischd A, et al. In vitro and in vivo corrosion measurements of magnesium alloys. Biomaterials 2006;27:1013–8.
[4] Zhang E, Xu L, Yang K. Formation by ion plating of Ti-coating on pure Mg for biomedical applications. Scr Mater 2005;53:523–7.
[5] Song G. Control of biodegradation of biocompatible magnesium alloys. Corros Sci 2007;49:1696–701.
[6] Gu XN, Xie XH, Li N, Zheng YF, Qin L. In vitro and in vivo studies on a Mg–Sr binary alloy system developed as a new kind of biodegradable metal. Acta Biomater 2012;8:2360–74.
[7] Li Z, Gu X, Lou S, Zheng Y. The development of binary Mg–Ca alloys for use as biodegradable materials within bone. Biomaterials 2008;29:1329–44.
[8] Gu XN, Li N, Zhou WR, Zheng YF, Zhao X, Cai QZ, et al. Corrosion resistance and surface biocompatibility of a microarc oxidation coating on a Mg–Ca alloy. Acta Biomater 2011;7:1880–9.
[9] Gu XN, Zheng YF, Lan QX, Cheng Y, Zhang ZX, Xi TF, et al. Surface modification of an Mg–1Ca alloy to slow down its biocorrosion by chitosan. Biomed Mater 2009;4:044109.
[10] Chu PK. Plasma surface treatment of artificial orthopedic and cardiovascular biomaterials. Surf Coat Technol 2007;201:5601–6.
[11] Zhao Y, Wong SM, Wong HM, Wu SL, Hu T, Yeung KWK, et al. Effect of carbon and nitrogen plasma immersion ion implantation on in vitro and in vivo biocompatibility of titanium alloy. ACS Appl Mater Interfaces 2013;5:1510–6.
[12] Zhao Y, Wu GS, Pan HB, Yeung KWK, Chu PK. Formation and electrochemical behavior of al and O plasma-implanted biodegradable Mg-Y-RE alloy. Mater Chem Phys 2012;132:187–91.
[13] Wu GS, Xu RZ, Feng K, Wu SL, Wu ZW, Sun GY, et al. Retardation of surface corrosion of biomedical magnesium alloys by aluminum ion implantation. Appl Surf Sci 2012;258:7651–7.
[14] Zhao Y, Wu GS, Lu QY, Wu J, Xu R, Yeung KWK, et al. Improved surface corrosion resistance of WE43 magnesium alloy by dual titanium and oxygen ion implantation. Thin Solid Films 2013;529:407–11.
[15] Xin YC, Chu PK. In: Dong HS, editor. Surface engineering of light alloys – aluminium, magnesium and titanium alloys. Abington: CRC Press and Woodhead Publishing; 2010. p. 393. chap. 11.
[16] Ryu HS, Hong SH. Corrosion resistance and antibacterial properties of AG-containing MAO coatings on AZ31 magnesium alloy formed by microarc oxidation. J Electrochem Soc 2010;157:C131–6.
[17] Petrini P, Arciola CR, Pezzali I, Bozzini S, Montanaro L, Tanzi MC, et al. Antibacterial activity of zinc modified titanium oxide surface. Int J Artif Organs 2006;29:434–42.
[18] Fang SJ, Liu YH, Diao LH, Yu SR, Zhang J. Influence of Cu^{2+} on sulfate-reducing bacteria associated with magnesium alloy. ISIJ Int 2007;47:1647–51.
[19] Zheng YF, Liu D, Liu XL. Enhanced corrosion resistance of Zr coating on biomedical TiNi alloy prepared by plasma immersion ion implantation and deposition. Appl Surf Sci 2008;55:512–4.
[20] Xue XY, Chu CL, Yin LH, Pu YP, Chu PK. Cytocompatibility and haemocompatibility of Zr, ZrC and ZrCN films. Surf Eng 2012;28:448–52.
[21] Yasuyuki M, Kunihiro K, Kurissery S, Kanavillil N, Sato Y, Kikuchi Y. Antibacterial properties of nine pure metals: a laboratory study using *Staphylococcus aureus* and *Escherichia coli*. Biofouling 2010;26:851–8.
[22] Liu XY, Huang AP, Ding CX, Chu PK. Bioactivity and cytocompatibility of zirconia (ZrO_2) films fabricated by cathodic arc deposition. Biomaterials 2006;27:3904–11.
[23] Scarano A, Piattelli M, Caputi S, Favero G, Piattelli A. Bacterial adhesion on commercially pure titanium and zirconium oxide disks: an in vivo human study. J Periodontol 2004;75:292–6.
[24] Al-Radha ASD, Dymock D, Younes C, O'Sullivan D. Surface properties of titanium and zirconia dental implant materials and their effect on bacterial adhesion. J Dent 2012;40:146–53.
[25] Manicone PF, Lommetti PR, Raffaelli L. An overview of zirconia ceramics: basic properties and clinical applications. J Dent 2007;35:819–26.
[26] Kokubo T, Kushitani H, Sakka S, Kitsugi T, Yamamuro T. Solutions able to reproduce in vivo surface-structure changes in bioactive glass-ceramic A-W. J Biomed Mater Res 1990;24:721–34.
[27] Fischer J, Pröfrock D, Hort N, Willumeit R, Feyerabend F. Improved cytotoxicity testing of magnesium materials. Mater Sci Eng B 2011;176:1773–7.
[28] Chu PK. Recent developments and applications of plasma immersion ion implantation (PIII). J Vac Sci Technol B 2004;22:289–96.
[29] Xin YC, Hu T, Chu PK. Degradation behavior of pure magnesium in simulated body fluids with different concentrations of HCO_3^-. Corros Sci 2011;53:1522–8.
[30] Zhao Y, Wu GS, Jiang J, Wong HM, Yeung KWK, Chu PK. Improved corrosion resistance and cytocompatibility of magnesium alloy by two-stage cooling in thermal treatment. Corros Sci 2012;59:360–5.
[31] Liu CL, Xin YC, Tian XB, Chu PK. Degradation susceptibility of surgical magnesium alloy in artificial biological fluid containing albumin. J Mater Res 2007;22:1806–14.
[32] Arciola CR, Alvi FI, An YH, Campoccia D, Montanaro L. Implant infection and infection resistant materials: a mini review. Int J Artif Organs 2005;28:1119–25.
[33] Wu SL, Liu XM, Yeung A, Yeung KWK, Kao RYT, Wu GS, et al. Plasma-modified biomaterials for self-antimicrobial applications. ACS Appl Mater Interfaces 2011;3:2851–60.
[34] Quirynen M, Bollen C. The influence of surface roughness and surface-free energy on supra- and subgingival plaque formation in man. A review of the literature. J Clin Periodontol 1995;22:1–14.
[35] Rabea EI, Badawy MET, Stevens CV, Smagghe G, Steurbaut W. Chitosan as antimicrobial agent: applications and mode of action. Biomacromolecules 2003;4:1457–65.
[36] Cao HL, Liu XY, Meng FH, Chu PK. Biological actions of silver nanoparticles embedded in titanium controlled by micro-galvanic effects. Biomaterials 2011;32:693–705.
[37] Song YW, Shan DY, Chen RS, Zhang F, Han EH. Biodegradable behaviors of AZ31 magnesium alloy in simulated body fluid. Mater Sci Eng C 2009;29:1039–45.
[38] Witte F, Hort N, Vogt C, Cohen S, Kainer KU, Willumeit R, et al. Degradable biomaterials based on magnesium corrosion. Curr Opin Solid State Mater Sci 2008;12:63–72.